

<https://doi.org/10.1038/s44310-024-00043-4>

Enhancing X-ray generation from twisted multilayer van der Waals materials by shaping electron wavepackets

Check for updates

Lee Wei Wesley Wong & Liang Jie Wong

We study twisted bilayer van der Waals (vdW) materials as a platform to generate versatile bremsstrahlung X-rays, and show that the twist angle in bilayer vdW materials provides an unprecedented degree of controllability over various properties of bremsstrahlung radiation from these materials. Specifically, we combine the waveshaping of the free electron's quantum wavepacket with the unique crystalline atomic positioning of twisted bilayers to realize shaped bremsstrahlung X-rays, which feature enhancements in directionality and intensity. In the process, we present a theoretical model for bremsstrahlung radiation that is applicable to twisted multilayer vdW materials in general. We also investigate the dependence of our X-ray emission mechanism on physical parameters, including the interlayer spacing and number of layers. Our findings pave the way for the use of twisted multilayer van der Waals materials in the generation of tailored X-ray spectra for applications like X-ray imaging, X-ray fluorescence, and X-ray treatment.

Bilayer van der Waals (vdW) materials are an emerging class of materials whose name is derived from the fact that they comprise two layers of two-dimensional materials bonded by weak vdW attractive force. Twisted bilayer vdW materials are formed when these two atomic layers are twisted at different orientations with respect to each other, which can cause significant changes in their optoelectronic properties. One of the most popular twisted bilayer vdW materials is twisted bilayer graphene (TBG). At certain so-called magic twist angles, the optoelectronic properties of TBG are substantially altered, leading to important phenomena such as superconductivity, interaction-induced insulating states, extremely flat bands, etc.^{1–9}. Bilayer transition metal dichalcogenides (TMDs) vdW materials like WSe₂, WS₂, MoSe₂, and MoS₂ at magic twist angles possess unique optoelectrical properties that closely depend on their chemical composition^{10–20}. Research on twisted bilayer vdW materials has revealed their enormous potential to improve the performance of optoelectronic devices, including photodetectors^{21,22}, integrated circuits^{23,24}, photovoltaic cells²⁵, light-emitting diodes²⁶, and nanolaser²⁷. Recent development of fabrication techniques at the atomic scale has further advanced the engineering of twisted multilayer vdW materials, leading to the birth of twistronics, which aims to control and exploit unique physical phenomena emerging at magic twist angles between multiple adjacent layers^{28–40}.

Whereas TBG, twisted bilayer TMDs and twisted multilayer vdW heterostructure have been extensively studied for a variety of applications in the optical regime, the study of these materials as free electron-driven

sources of X-rays remains to be undertaken. Specifically, the role of the twisting geometry in bilayer vdW materials for free electron-driven light emission in these materials, especially in the hard X-ray regime, has yet to be explored. X-rays are essential tools in cutting-edge modern science and industry for applications such as X-ray spectroscopy^{41,42}, X-ray crystallography^{43–45}, X-ray computed tomography⁴⁶, materials characterization⁴⁷, etc. X-rays also serve life-saving purposes in the medical sector in the form of radiography and radiotherapy^{48–50}, providing critical health information and treatments for diseases like cancer. Conventional X-ray sources such as X-ray tubes are limited in tunability, whereas more expensive devices like synchrotron can generate tunable X-ray but is generally massive. This has motivated efforts to find innovative solutions for more versatile sources of tabletop X-rays.

The unprecedented study of free electron-driven twisted multilayer materials as X-ray sources, which is the topic of this paper, is further motivated by a rich field of research in free electron-driven X-ray sources. This includes free electrons propagating through a vdW single-crystals and heterostructures which comprise multiple atomic layers vertically stacked upon each other, have opened a new gate to generate tunable X-ray^{51–58}. Other noteworthy X-ray generation mechanisms include Smith–Purcell emitters^{59–61}, light wells⁶², free-electron lasers^{63–65}, inverse Compton scattering^{66,67}, high-harmonic generation^{68–71}, plasmon polaritons⁷² and vacuum forces⁷³. These studies have been expanded to explore the effects of electron waveshaping as a robust means of tailoring various quantum

School of Electrical and Electronic Engineering, Nanyang Technological University, 50 Nanyang Avenue, Singapore, 639798, Singapore.

 e-mail: liangjie.wong@ntu.edu.sg

electrodynamics (QED) processes^{74–81}. For example, the directionality and intensity of free electron X-rays generated from vdW materials can be tailored, by shaping the electron wavepackets to spatially overlap with the atomic lattice⁸¹. The shaping of electron spatio-temporal profile can be achieved using static field^{82–85}, laser pulses^{86–89}, surface plasmon polaritons (SPPs)⁹⁰, phase masks and programmable phase plates^{91–95}.

In this paper, we investigate the use of the twisted bilayer vdW materials as target materials in free electron-driven X-ray generation. We present an ab initio theoretical model for bremsstrahlung radiation that is applicable to twisted multilayer vdW materials in general. Using this model, we show that the twist angle can be used as a mean to control the relative positions of atomic centers in the crystal, allowing a broad range of possible X-ray profiles to be achieved. Furthermore, this can be combined with the shaping of the free electron’s quantum wavefunction to create X-ray sources that are highly versatile. We show that by twisting the bilayer vdW materials, we are able to control the output X-ray properties to feature enhanced directionality or enhanced intensity. We then extend our study to multilayer vdW materials with different interlayer spacings, i.e., the separation between consecutive atomic layers. Our results reveal that smaller interlayer spacing leads to slower fluctuations with greater shifts in the X-ray emission profile (with respect to X-ray energy and emission angle). We show that the output X-ray intensity scales up as an increasing number of atomic layers in the twisted multilayer vdW materials, providing an intuitive and effective way to enhance the output X-ray intensity for any shaped X-ray output profile of choice. Our results should pave the way for the use of twisted bilayer and multilayer materials in X-ray generation for X-ray imaging and other applications in areas including medicine, industry, security and fundamental science.

Results

Analytical QED model of bremsstrahlung from twisted multilayer vdW materials

When a free electron is deflected by an atomic potential, the free electron loses energy in the form of bremsstrahlung radiation. X-rays in bremsstrahlung radiation form the basis of our X-ray generation mechanism. Throughout our entire work, we model the bremsstrahlung scattering process based on first principles from quantum electrodynamics (QED). We model the shaped electron wavefunction Ψ_p , approximating a Bessel beam of order 1⁸¹, using 6 momentum eigenstates:

$$\Psi_p(x) = \sum_{m=1}^6 \frac{e^{i(m-1)\frac{2\pi}{6}}}{\sqrt{6}} u^\uparrow(p_m) e^{-i\mathbf{p}_m^\mu x_\mu} \quad (1)$$

where $u^\uparrow(p) e^{-i\mathbf{p}^\mu x_\mu}$ is the Dirac equation’s planewave solution for a single free electron in a definite momentum eigenstate, $u^\uparrow(p) = [\sqrt{p^0} \bar{\sigma}_\mu \xi^\uparrow, \sqrt{p^0} \sigma_\mu \xi^\uparrow]^T / \sqrt{2p^0}$ the Dirac u-type spinor, $\sigma^\mu = \{1, \sigma_x, \sigma_y, \sigma_z\}$, $\bar{\sigma}^\mu = \{1, -\sigma_x, -\sigma_y, -\sigma_z\}$, $\sigma_{x,y,z}$ the 2×2 Pauli matrices, ξ^s the spinor where $\xi^\uparrow = [1, 0]^T$ represents spin-up ($\xi^\downarrow = [0, 1]^T$ spin-down), \hbar the reduced Planck constant, p^μ the four-momenta, x_μ the spacetime four-vector, and the repeated index convention $p^\mu x_\mu = p^0 x_0 - \mathbf{p} \cdot \mathbf{x}$ (bold variables denote the three-vector components). The four-momentum p_m for each electron momentum state is given by

$$p_m = \left\{ \frac{E_p}{c}, |\mathbf{p}| \sin[\theta_p] \cos[\phi_{p,m}], |\mathbf{p}| \sin[\theta_p] \sin[\phi_{p,m}], |\mathbf{p}| \cos[\theta_p] \right\} \quad (2)$$

where E_p is the electron energy, $|\mathbf{p}|$ the electron momentum magnitude satisfying the energy dispersion relation $E_p^2 = |\mathbf{p}|^2 c^2 + m_e^2 c^4$ (c is the speed of light in free space and m_e the electron mass), θ_p the polar (incident) angle and $\phi_{p,m} = (m - 1)2\pi/6$ the azimuthal angle. The electron’s probability distribution function $\Psi_p^\dagger \Psi_p$ (i.e., electron spatial profile) is specifically shaped to possess identical periodicity as the atomic layer’s lattice vectors (in

the xy -plane) while remains invariant along the electron’s main propagating direction (the z -axis).

The total Yukawa potential (in Fourier space \mathbf{k}) of atoms that contribute effectively to the output bremsstrahlung in a twisted N_1 -layer vdW material (with interlayer spacing $d_z = |\mathbf{d}_z|$) is modeled as

$$A_{\text{Yu,Twi}}(\mathbf{k}; N_1, \mathbf{d}_z) = \sum_{l=1}^{N_1} e^{i(l-1)\mathbf{k} \cdot \mathbf{d}_z} a_{\text{Yu},l}(\mathbf{k}; \phi_{\text{Twi},l}), \quad (3)$$

with Yukawa potential from l^{th} -layer $a_{\text{Yu},l}(\mathbf{k}; \phi_{\text{Twi},l})$ oriented at twist angle $\phi_{\text{Twi},l}$ as

$$a_{\text{Yu},l}(\mathbf{k}; \phi_{\text{Twi},l}) = \sum_{n_l=1}^{N_{a,l}} \left[\frac{-Z_{n_l} q_e}{\epsilon_0} e^{i\mathbf{k} \cdot [\hat{R}(\phi_{\text{Twi},l}) \mathbf{d}_{n_l}]} \left(\sum_{j_n} \frac{C_{j_n}}{\left(\frac{\mu_{j_n}}{a_0}\right)^2 + |\mathbf{k}|^2} \right) \right] \quad (4)$$

where q_e is the electron charge, ϵ_0 the vacuum permittivity, a_0 the Bohr radius, $N_{a,l}$ the total number of atoms in l^{th} atomic layer, $\hat{R}(\phi_{\text{Twi},l})$ the rotation matrix, \mathbf{d}_{n_l} the lattice vector of n_l^{th} atom, Z_{n_l} the atomic number of n_l^{th} atom associated with screening function parameters C_{j_n} and μ_{j_n} analytically fitted to Dirac-Hartree-Fock-Slater (DHFS) self-consistent data given in refs. 96,97. Details regarding \mathbf{d}_{n_l} , $\hat{R}(\phi_{\text{Twi},l})$ and Z_{n_l} , C_{j_n} , μ_{j_n} are discussed in Methods.

The bremsstrahlung differential cross section involving a shaped electron wavepacket (comprising N_s discrete momentum states associated with normalized coefficient c_m) and a twisted N_1 -layer vdW material (with interlayer spacing $d_z = |\mathbf{d}_z|$) is given by

$$\frac{d\sigma}{d\omega_{k'} d\Omega_{k'}} = \sum_{r',s'} \int d\Omega_{p'} \delta_{E_p - \hbar\omega_{k'} - E_{p'}} \frac{\omega_{k'} |\mathbf{p}'|}{8\epsilon_0 (2\pi)^5 \hbar^3 c^5 |\mathbf{p}|} \times \left| \sum_{m=1}^{N_s} c_m \left[\sum_{l=1}^{N_1} e^{i(l-1)\mathbf{\kappa}_m \cdot \mathbf{d}_z} a_{\text{Yu},l}(\mathbf{\kappa}_m; \phi_{\text{Twi},l}) \right] \left[\mathcal{M}_{k'p'p_m}^{r's'\uparrow} \right] \right|^2 \quad (5)$$

where σ is the bremsstrahlung cross section, $\omega_{k'}$ is the angular frequency and $\hbar k'^\mu$ is the four-momenta of the output photon with energy $\hbar\omega_{k'} = \hbar k'^0 c$ and three-momenta $\hbar \mathbf{k}' = |\hbar \mathbf{k}'| \{ \sin \theta_{k'} \cos \phi_{k'}, \sin \theta_{k'} \sin \phi_{k'}, \cos \theta_{k'} \}$, $\theta_{k'}$ (polar angle) and $\phi_{k'}$ (Azimuthal angle) are the photon emission angles and $\Omega_{k'}$ the solid angle. p'^μ is the four-momenta of the output electron with energy $E_{p'} = \sqrt{|\mathbf{p}'|^2 c^2 + m_e^2 c^4}$, three-momenta $\mathbf{p}' = |\mathbf{p}'| \{ \sin \theta_{p'} \cos \phi_{p'}, \sin \theta_{p'} \sin \phi_{p'}, \cos \theta_{p'} \}$ and solid angle $\Omega_{p'}$. Unitless Kronecker delta $\delta_{E_p - \hbar\omega_{k'} - E_{p'}}$ represents the energy constraint and wavevector $\mathbf{\kappa}_m = \frac{\mathbf{p}_m}{\hbar} - \mathbf{k}' - \frac{\mathbf{p}'}{\hbar}$.

The scattering amplitude $\mathcal{M}_{k'p'p_m}^{r's'\uparrow}$ is given by

$$\mathcal{M}_{k'p'p_m}^{r's'\uparrow} = -i q_e^2 \left\{ \sqrt{2p'^0} u^{s'}(p') \right\}^\dagger \left\{ \gamma^0 (\gamma^\sigma \epsilon_\sigma^{r'*}) \frac{\gamma^{\nu} (\mathbf{p}' - \hbar \mathbf{k}')_\nu + m_e c I}{2(p')^\mu (\hbar k')_\mu} \gamma^0 \right. \\ \left. + \frac{\gamma^{\nu} (\mathbf{p}_m - \hbar \mathbf{k}')_\nu + m_e c I}{-2(p_m)^\mu (\hbar k')_\mu} (\gamma^\sigma \epsilon_\sigma^{r'*}) \right\} \left\{ \sqrt{2p^0} u^\uparrow(p_m) \right\} \quad (6)$$

where $u^{s'}(p')$ the output electron’s Dirac u-type spinor with spin s' , $\epsilon_\sigma^{r'}$ the photon polarization and γ^σ the gamma matrices following conventions of Peskin and Schroeder⁹⁸ (e.g., metric tensor with diagonal elements $\{1, -1, -1, -1\}$).

Tailoring X-ray emission profiles

We first present how shaping the electron wavepacket and twisting the bilayer vdW materials (graphene and WS₂) can tailor the bremsstrahlung differential cross section $d\sigma/(d\omega_{k'} d\Omega_{k'})$, which is proportional to the output X-ray intensity. Figure 1a, f illustrate the bottom views of twisted

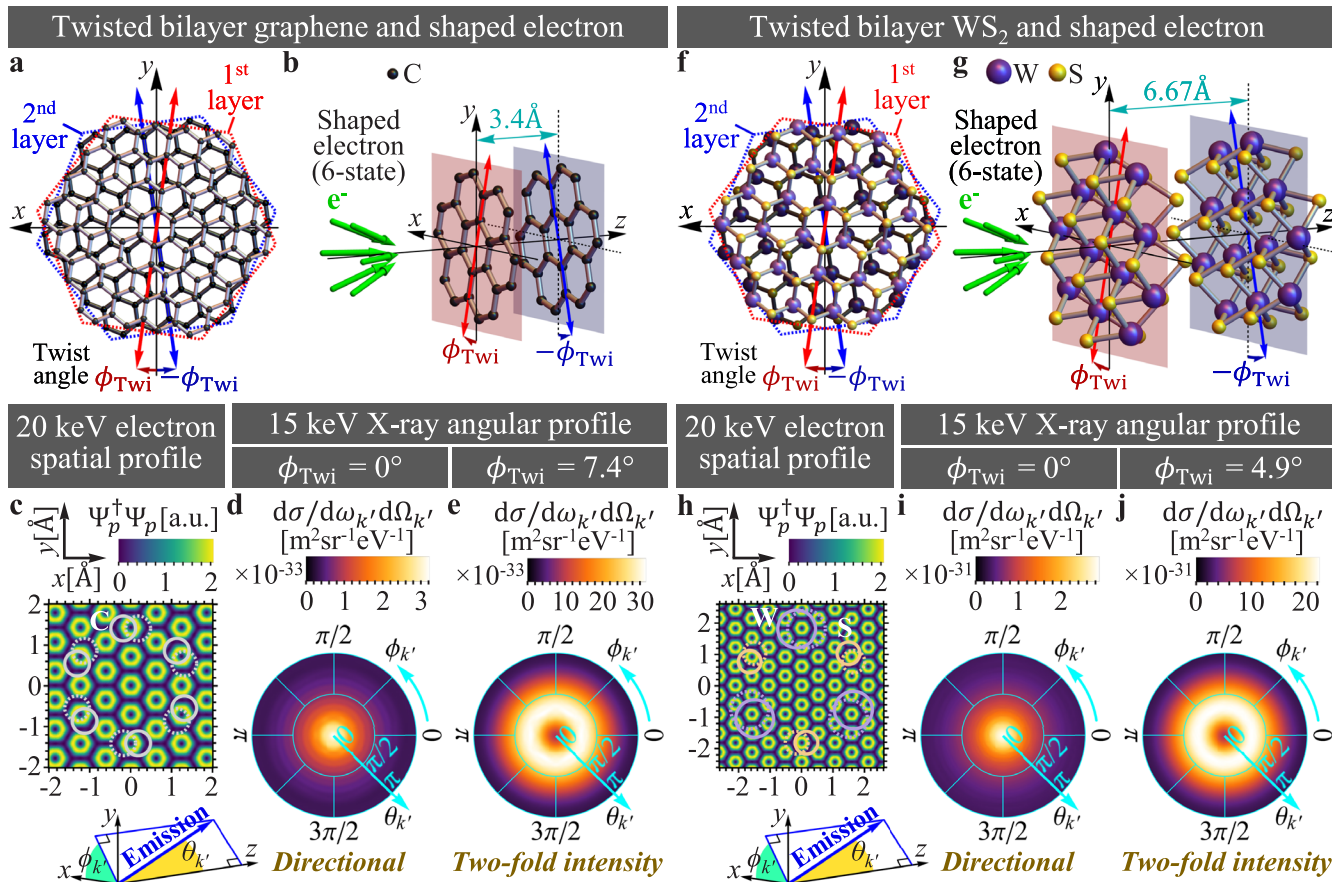


Fig. 1 | Tailoring bremsstrahlung via electron waveshaping and twisted bilayer vdW materials. **a** Illustrates the bottom view of a twisted bilayer graphene which the two atomic layers (lies in the xy -plane) are twisted in opposite orientation at twist angle ϕ_{twi} . **b** Depicts a 20 keV single-shaped electron wavefunction (6-state, incident angle $\theta_p = 8.03^\circ$) propagating in the z -axis toward a twisted bilayer graphene. **c** Shows the shaped electron spatial profile (probability distribution function $\Psi_p^\dagger \Psi_p$) with periodic patterns, where solid (dashed) gray circles denoting the projections of effective carbon atoms in the first (second) layer. The output 15 keV X-ray angular profiles (differential cross section $d\sigma/(d\omega_{k'} d\Omega_{k'})$) are shown in **(d, e)** for twist angles of 0° and 7.4° , respectively. **f** Illustrates the bottom view of a twisted bilayer WS_2 and

g Depicts a 20 keV single-shaped electron wavefunction (6-state, incident angle $\theta_p = 9.42^\circ$) propagating in the z -axis towards a twisted bilayer WS_2 . Its spatial profile is shown in **(h)** where solid (dashed) purple and yellow circles denoting the projections of effective tungsten and sulfur atoms in the first (second) layer, respectively. The output 15 keV X-ray angular profiles (differential cross section $d\sigma/(d\omega_{k'} d\Omega_{k'})$) are shown in **(i, j)** for twist angles of 0° and 4.9° , respectively. For different twist angle, shaped electron incident on bilayer vdW materials can emit X-ray with either unidirectionality **(d, i)** or enhanced intensity **(e, j)**, compared to unshaped electron cases.

bilayer graphene (TBG) and twisted bilayer WS_2 at twist angle $\phi_{\text{twi},i}$ respectively. Figures 1b, g depict physical configurations of single 6-state shaped electron wavepacket incident on a TBG and a twisted bilayer WS_2 , respectively. The TBG has interlayer spacing of 3.4 \AA while the twisted bilayer WS_2 has a longer interlayer spacing of 6.67 \AA . The electron spatial profiles (probability distribution function $\Psi_p^\dagger \Psi_p$) are engineered to form periodic patterns matching the untwisted bilayer graphene and untwisted bilayer WS_2 lattice periodicities, as shown in Fig. 1c, h, respectively. Figure 1d, e show the output 15 keV X-ray angular profiles for bilayer graphene with $\phi_{\text{twi},i}$ of 0° (untwisted) and 7.4° (twisted), respectively. Figure 1i, j show the output 15 keV X-ray angular profiles for bilayer WS_2 with $\phi_{\text{twi},i}$ of 0° (untwisted) and 4.9° (twisted), respectively. In both untwisted cases (Fig. 1d, i), the shaped electron wavepacket generates X-ray with unidirectionality, i.e., intensity peaks in singular forward direction, compared to cases with unshaped electron wavepacket (Supplementary Information Section 1, Fig. S1). Using the same shaped electron wavepacket, twisting the bilayer vdW materials to specific twist angles (Fig. 1e, j) restores the X-ray directionality but at the same time induces a two-fold enhancement in the X-ray intensity. Also, notice that the bremsstrahlung differential cross section is generally proportional to the square of the atomic number, which explains the much higher X-ray intensity from bilayer WS_2 compared to that of bilayer graphene. One can refer to Fig. S2 in Supplementary

Information Section 2 to understand the X-ray intensity's dependence on the twist angle of bilayer vdW material, which the optimal twist angles associated with the highest output X-ray intensity are obtained accordingly. Another interesting aspect is the polarization of generated X-rays, which some important examples are presented in Supplementary Information Section 3.

X-ray intensities' dependence on interlayer spacing and number of layers

Next, we investigate the role of interlayer spacing d_z in controlling the output X-ray intensity. For simplicity, we consider two carbon atoms aligned on the z -axis in both cases of single 1-state unshaped electron wavepacket ("1-S") and a single 6-state shaped electron wavepacket ("6-S"), as depicted in Fig. 2a, d, respectively. The corresponding X-ray emission maps for "1-S" ("6-S") with d_z of 1 and 3 \AA are shown in Fig. 2b, c (Fig. 2e, f), respectively. Similar to previous results, unshaped electron wavepacket emits X-ray with intensity peaks at large emission angles ($>45^\circ$), while shaped electron wavepacket generates more directional X-ray (emitted mostly in the z -direction). It is observed that in all cases, smaller interlayer spacing results in fluctuations (with respect to X-ray energy and emission angle) with lower frequency and greater amplitude, which appear as wider fringes in the X-ray emission map.

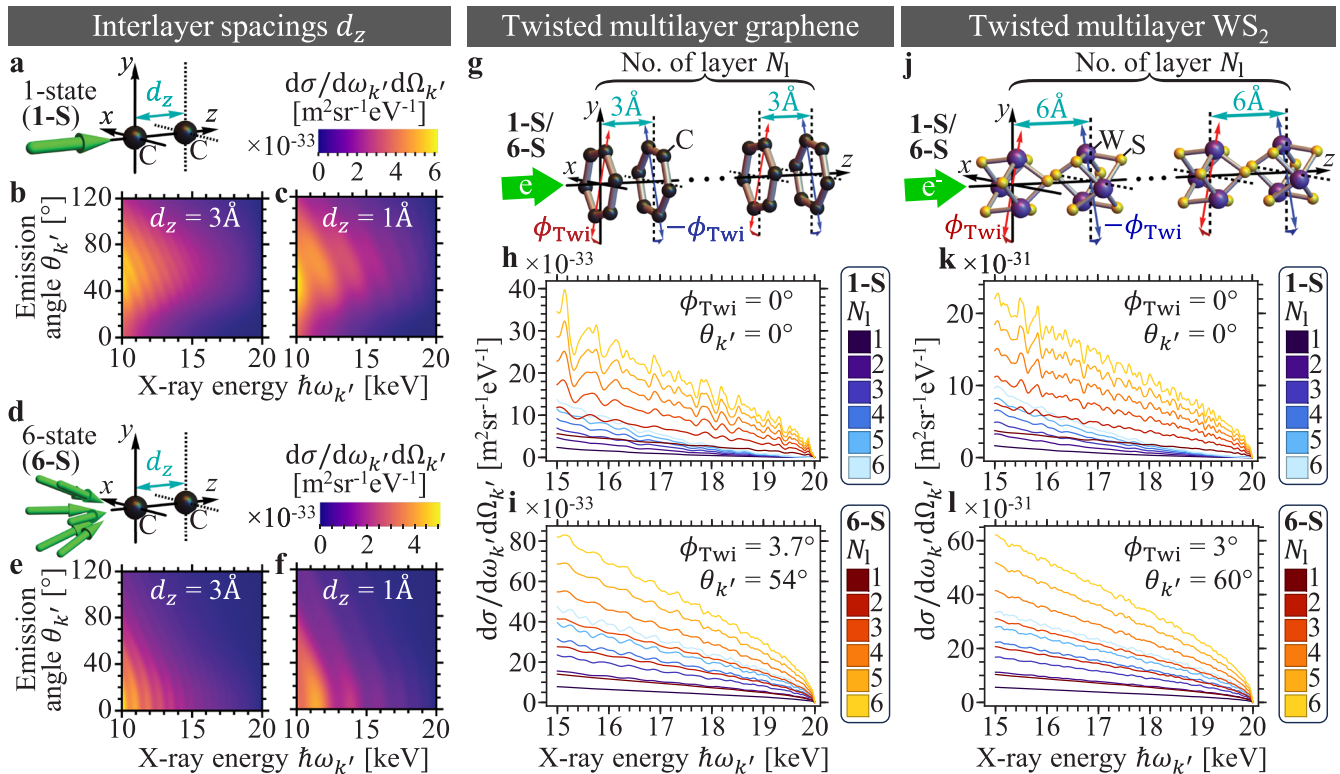


Fig. 2 | Enhancement in X-ray intensities from twisted multilayer graphene and twisted multilayer WS₂. **a** Illustrates a 20 keV single unshaped electron wavefunction (1-state) propagates toward two carbon atoms aligned along the z-axis with interlayer spacing d_z . **b, c** Show the colormaps (emission angle $\theta_{k'}$ against X-ray energy $E_{k'}$) of the bremsstrahlung differential cross section $d\sigma/(d\omega_{k'}d\Omega_{k'})$ for $d_z = 3\text{ \AA}$ and $d_z = 1\text{ \AA}$, respectively. Similarly, **(d)** illustrates a 20 keV single-shaped electron wavefunction (6-state, incident angle $\theta_p = 15^\circ$) and **e, f** show the corresponding X-ray emission maps for $d_z = 3\text{ \AA}$ and $d_z = 1\text{ \AA}$, respectively. Comparing **(c, f)** and **(b, e)**, shorter interlayer spacing induces slower fluctuations in the X-ray

emission map (with respect to X-ray energy and emission angle). **g** Depicts a 20 keV electron incident on twisted N_1 -layer graphene ($d_z = 3\text{ \AA}$). **(h, i)** Show the output X-ray intensity scales up with increasing N_1 for both unshaped “1-S” and shaped “6-S” (incident angle $\theta_p = 16.22^\circ$) electron wavepackets, at twist angles ϕ_{Twist} of 0° (emission angle $\theta_{k'} = 0^\circ$) and 3.7° ($\theta_{k'} = 54^\circ$), respectively. **j** Illustrates 20 keV electron incident on twisted N_1 -layer WS₂ ($d_z = 6\text{ \AA}$). **k, l** Show the output X-ray intensity scales up with increasing N_1 for both “1-S” and “6-S” ($\theta_p = 15.77^\circ$) electron wavepackets, at ϕ_{Twist} of 0° ($\theta_{k'} = 0^\circ$) and 3° ($\theta_{k'} = 60^\circ$), respectively.

We now extend our studies to twisted multilayer graphene and twisted multilayer WS₂, which their corresponding physical configurations are illustrated in Fig. 2g, j, respectively. The atomic layers are twisted alternatively in opposite orientation, i.e., for twist angle ϕ_{Twist} the l th-layer is twisted at $(-1)^{l-1}\phi_{\text{Twist}}$. The output X-ray differential cross sections for twisted multilayer graphene at different X-ray energies (for both “1-S” unshaped electron wavepacket and “6-S” shaped electron wavepacket) are plotted in Fig. 2h (untwisted $\phi_{\text{Twist}} = 0^\circ$, emission angles $\theta_{k'} = \phi_{k'} = 0^\circ$) and 2i (twisted $\phi_{\text{Twist}} = 3.7^\circ$, emission angles $\theta_{k'} = 54^\circ$, $\phi_{k'} = 0^\circ$). The corresponding plottings for twisted multilayer WS₂ are presented in Fig. 2k (untwisted $\phi_{\text{Twist}} = 0^\circ$, emission angles $\theta_{k'} = \phi_{k'} = 0^\circ$) and 2l (twisted $\phi_{\text{Twist}} = 3^\circ$, emission angles $\theta_{k'} = 60^\circ$, $\phi_{k'} = 0^\circ$). In all cases, the output X-ray intensities always scale up as the number of layers N_1 , even in lower energy regime down to 5 keV (shown in Supplementary Information Section 4). Compared to twisted multilayer graphene with shorter interlayer spacing of 3 \AA , the fluctuations in X-ray intensity (with respect to X-ray energy) for twisted multilayer WS₂ oscillate faster with lower amplitude due to a longer interlayer spacing of 6 \AA , which is consistent with previous findings. One can also observe that in both cases of graphene and WS₂, the fluctuations in X-ray intensities (with respect to X-ray energy) tend to vanish at larger twist angle, due to misalignment of atomic potentials along the longitudinal direction.

Discussion

To study shaped free electron radiation from twisted bilayer vdW materials, we adopt the “double-twisting” model, wherein the two atomic layers are twisted in opposite orientations simultaneously. This model preserves the

geometrical angular symmetry in the xy -plane for mathematical convenience, and allows one to control the symmetry of the output X-ray emission profile. Due to the hexagonal lattice structure of the graphene and WS₂, we choose to use shaped electron wavepacket comprising 6 specific momentum states with identical incident angle θ_p . The electron spatial profile can thus be conveniently engineered via varying θ_p to match the lattice vectors of different bilayer vdW materials. The electron spatial profile is invariant along the z-axis, i.e., longitudinally identical in the vicinity of every effective atomic centers of the vdW materials. This guarantees the optimization of the desired output X-ray emission profile by eliminating unwanted interference due to a mismatch between the electron spatial profile and atomic potentials.

The emergence of fluctuations in the output bremsstrahlung X-ray emission map with respect to X-ray energy and emission angle is fully deterministic, i.e., not due to noise or other sources of randomness, but instead a signature of the interference between the atomic potentials in Fourier space, which mathematically translate to expressions of phasors in Eqs. (3) and (4). The frequency and amplitude of the fluctuations are shown to be sensitive to the interlayer spacing between the atomic layers in vdW materials, but they do not significantly alter the overall directionality of the output X-ray. Although these fluctuations are affected by the interlayer spacing, to our best knowledge, in this paper, there is no intuitive way to precisely manipulate them. Nevertheless, future works can be carried out to model these fluctuations, which we believe can lead to even stronger output radiation under coherent control of relevant constructive interference.

Let us now address the importance of the twisting geometry of the bilayer vdW materials. At certain choices of twist angle, the atomic centers of the atoms (carbon for bilayer graphene, tungsten and sulfur for bilayer WS₂) tend to align with the intensity peaks of the shaped electron’s spatial profile, and thus lead to the transformation of the X-ray emission profile from “unidirectional” mode to “intensity-enhanced” mode. On the contrary, for an unshaped electron wavepacket, twisting the bilayer vdW materials does not induce any significant change due to the uniform distribution of electron spatial profile (shown in Supplementary Information Section 1 Fig. S1). Therefore, both twisted bilayer vdW materials and shaped electron wavepacket are essential to realize the “transformation” phenomenon of the output X-ray profile. The twisting geometry provides greater control over tunable X-ray, especially in the scenario where only a certain shaped electron wavepacket is available. Moreover, the twisting of vdW materials generally does not occupy extra operational spaces, which could be advantageous comparing to tunable PXR, which sometimes requires tilting of the crystal.

Additionally, the twisting geometry of bilayer vdW materials can also be used to control the polarization of the generated X-ray, which is an important feature that can potentially lead to a wide range of applications. As presented in Supplementary Information Section 3, our results provide a first glimpse of how a combination of shaped electron wavefunction and twisted bilayer crystal can transform the X-ray from circular polarization to linear polarization (or the other way around). A more quantitative mechanism based on bilayer materials to tailor X-ray polarization is yet to be studied and is not within the scope of this paper, but we believe it deserves to be explored in more detail in future work.

In conclusion, our studies on twisted bilayer and multilayer vdW materials with shaped electron wavepackets have led us to present a versatile method of tailoring bremsstrahlung X-rays. Based on first principles QED, we have computed the bremsstrahlung differential cross section considering arbitrarily shaped electron wavepackets and multilayer vdW heterostructure with arbitrary twisting geometries. Apart from shaping the electron wavepacket, the twisting geometry of vdW materials can provide extra degrees of freedom to tailor free electron radiation. By increasing the twist angle between two adjacent atomic layers, the output X-ray profiles can be transformed from “directional” mode to “intensity-enhanced” mode. This is due to the change of overlap conditions between the atomic centers and electron probability distribution. We have outlined the importance of having a non-uniform electron spatial profile, i.e., shaped electron wavepacket, which is crucial for achieving such transformation. Significantly, we have extended our studies to twisted multilayer vdW materials. Our results show that it is feasible to scale up the output X-ray emission by increasing the number of twisted atomic layers, while preserving its transformation features as seen in twisted bilayer vdW materials. Our work also investigated the dependence of interlayer spacing of multilayer vdW materials, showing that a decrease in interlayer spacing results in greater but slower fluctuations in the output X-ray intensity as a function of X-ray energy and emission angle. These fluctuations tend to vanish at large twist angles, due to misalignment of atomic centers across different layers. Our findings show how the combination of free electron waveshaping and twisted multilayer materials can result in enhanced control over the output of X-ray sources, for applications ranging from medical imaging to industrial inspection.

Methods

Multilayer graphene

The lattice basis vectors of multilayer hexagonal crystalline structure are modeled as

$$\mathbf{a} = \{a, 0, 0\}, \mathbf{b} = \left\{ -\frac{1}{2}a, \frac{\sqrt{3}}{2}a, 1 \right\}, \mathbf{c} = \{0, 0, d_z\}, \quad (M1)$$

where a is the lattice constant ($a = 2.46 \text{ \AA}$ for graphene, $a = 3.15 \text{ \AA}$ for WS₂) and d_z is the interlayer spacing.

For each layer of graphene, there are two carbon atoms per unit cell. The lattice vectors of carbon atoms in n_l th unit cell of l th-layer graphene are

modeled as:

$$\mathbf{d}_{C,n_l} = a \left\{ \frac{1}{2}, \frac{\sqrt{3}}{6}, 0 \right\} + n_a \mathbf{a} + n_b \mathbf{b} + (l-1)\mathbf{c}, \quad (M2)$$

$$\mathbf{d}_{C,n_l} = a \left\{ 0, \frac{\sqrt{3}}{3}, 0 \right\} + n_a \mathbf{a} + n_b \mathbf{b} + (l-1)\mathbf{c}, \quad (M3)$$

where $a = 2.46 \text{ \AA}$, $n_a, n_b \in \mathbb{Z}$ and $l \in \mathbb{Z}^+$. The atomic number of carbon $Z_C = 6$ and screening parameters $C_{1,2} = \{0.1537, 8.0404\}$, $\mu_{1,2} = \{0.8463, 1.4913\}$ ^{96,97}.

Multilayer WS₂

For each layer of WS₂, there are one tungsten atom and two sulfur atoms per unit cell. The lattice vectors of tungsten atoms and sulfur atoms in n_l th unit cell of l th layer WS₂ are modeled as:

$$\mathbf{d}_{W_1,n_l} = a \left\{ 0, \frac{\sqrt{3}}{3}, 0 \right\} + n_a \mathbf{a} + n_b \mathbf{b} + (l-1)\mathbf{c}, \quad (M4)$$

$$\mathbf{d}_{S_1,n_l} = a \left\{ \frac{1}{2}, \frac{2\sqrt{3}}{3}, -\frac{1}{2} \right\} + n_a \mathbf{a} + n_b \mathbf{b} + (l-1)\mathbf{c}, \quad (M5)$$

$$\mathbf{d}_{S_2,n_l} = a \left\{ \frac{1}{2}, \frac{2\sqrt{3}}{3}, \frac{1}{2} \right\} + n_a \mathbf{a} + n_b \mathbf{b} + (l-1)\mathbf{c}, \quad (M6)$$

where $a = 3.15 \text{ \AA}$, $n_a, n_b \in \mathbb{Z}$ and $l \in \mathbb{Z}^+$. The atomic number of tungsten $Z_W = 74$ and screening parameters $C_{1,2,3} = \{0.15, 0.6871, 0.1629\}$, $\mu_{1,2,3} = \{28.63, 4.2426, 1.234\}$ ^{96,97}. The atomic number of sulfur $Z_S = 16$ and screening parameters $C_{1,2,3} = \{0.5459, -0.5333, 0.9874\}$, $\mu_{1,2,3} = \{6.3703, 2.5517, 1.6753\}$ ^{96,97}.

Rotation matrix

To model the twisting of multilayer vdW material in the xy -plane, we apply the rotation matrix $R(\phi_{\text{Twi},l})$ to the lattice vectors of atoms in l th-layer as

$$\hat{R}(\phi_{\text{Twi},l}) = \begin{bmatrix} \cos[\phi_{\text{Twi},l}] & -\sin[\phi_{\text{Twi},l}] & 0 \\ \sin[\phi_{\text{Twi},l}] & \cos[\phi_{\text{Twi},l}] & 0 \\ 0 & 0 & 1 \end{bmatrix}, \quad (M7)$$

where $\phi_{\text{Twi},l}$ is the twist angle for l th-layer of the vdW material. For mathematical convenience, we model the twist angle of bilayer vdW material as $\phi_{\text{Twi},1} = -\phi_{\text{Twi},2} = \phi_{\text{Twi}} \geq 0$, i.e., the relative angle between the two atomic layers is always $2\phi_{\text{Twi}}$. Similarly, the twisted multilayer vdW material has l th-layer oriented at twist angle $\phi_{\text{Twi},l} = (-1)^{l-1} \phi_{\text{Twi}}$, i.e., the relative angle between two adjacent atomic layers is $2\phi_{\text{Twi}}$.

Data availability

All data needed to evaluate the conclusions in the paper are present in the manuscript and/or the Supplementary Information.

Received: 26 March 2024; Accepted: 16 September 2024;

Published online: 26 October 2024

References

- Lopes dos Santos, J. M. B., Peres, N. M. R. & Castro Neto, A. H. Graphene bilayer with a twist: electronic structure. *Phys. Rev. Lett.* **99**, 256802 (2007).
- Andrei, E. Y. & MacDonald, A. H. Graphene bilayers with a twist. *Nat. Mater.* **19**, 1265–1275 (2020).
- Bistritzer, R. & MacDonald, A. H. Transport between twisted graphene layers. *Phys. Rev. B* **81**, 245412 (2010).

4. Suárez Morell, E. et al. Flat bands in slightly twisted bilayer graphene: tight-binding calculations. *Phys. Rev. B* **82**, 121407 (2010).
5. Cao, Y. et al. Unconventional superconductivity in magic-angle graphene superlattices. *Nature* **556**, 43–50 (2018).
6. Lu, X. et al. Superconductors, orbital magnets and correlated states in magic-angle bilayer graphene. *Nature* **574**, 653–657 (2019).
7. Kerelsky, A. et al. Maximized electron interactions at the magic angle in twisted bilayer graphene. *Nature* **572**, 95–100 (2019).
8. Choi, Y. et al. Electronic correlations in twisted bilayer graphene near the magic angle. *Nat. Phys.* **15**, 1174–1180 (2019).
9. Liu, X. et al. Tunable spin-polarized correlated states in twisted double bilayer graphene. *Nature* **583**, 221–225 (2020).
10. Devakul, T. et al. Magic in twisted transition metal dichalcogenide bilayers. *Nat. Commun.* **12**, 6730 (2021).
11. Serlin, M. et al. Intrinsic quantized anomalous hall effect in a moiré heterostructure. *Science* **367**, 900–903 (2020).
12. Wu, F., Lovorn, T., Tutuc, E. & MacDonald, A. H. Hubbard model physics in transition metal dichalcogenide moiré bands. *Phys. Rev. Lett.* **121**, 026402 (2018).
13. Wu, F. et al. Topological insulators in twisted transition metal dichalcogenide homobilayers. *Phys. Rev. Lett.* **122**, 086402 (2019).
14. Shabani, S. et al. Deep moiré potentials in twisted transition metal dichalcogenide bilayers. *Nat. Phys.* **17**, 720–725 (2021).
15. Zhang, Y., Liu, T. & Fu, L. Electronic structures, charge transfer, and charge order in twisted transition metal dichalcogenide bilayers. *Phys. Rev. B* **103**, 155142 (2021).
16. Zang, J. et al. Hartree-fock study of the moiré hubbard model for twisted bilayer transition metal dichalcogenides. *Phys. Rev. B* **104**, 075150 (2021).
17. Cazalilla, M. A. et al. Quantum spin hall effect in two-dimensional crystals of transition-metal dichalcogenides. *Phys. Rev. Lett.* **113**, 077201 (2014).
18. Zhang, Z. et al. Flat bands in twisted bilayer transition metal dichalcogenides. *Nat. Phys.* **16**, 1093–1096 (2020).
19. Wang, L. et al. Correlated electronic phases in twisted bilayer transition metal dichalcogenides. *Nat. Mater.* **19**, 861–866 (2020).
20. Vitale, V. et al. Flat band properties of twisted transition metal dichalcogenide homo- and heterobilayers of mos₂, mose₂, ws₂ and wse₂. *2D Mater.* **8**, 045010 (2021).
21. Ding, Y. et al. Stacking-mode confined growth of 2H-MoTe₂/MoS₂ bilayer heterostructures for UV–vis–IR photodetectors. *Nano Energy* **49**, 200–208 (2018).
22. Ye, L., Li, H., Chen, Z. & Xu, J. Near-infrared photodetector based on MoS₂/Black phosphorus heterojunction. *ACS Photonics* **3**, 692–699 (2016).
23. Radisavljevic, B., Whitwick, M. B. & Kis, A. Integrated circuits and logic operations based on single-layer MoS₂. *ACS Nano* **5**, 9934–9938 (2011).
24. Wang, H. et al. Integrated circuits based on bilayer MoS₂ transistors. *Nano Lett.* **12**, 4674–4680 (2012).
25. Chen, P. et al. Approaching the intrinsic exciton physics limit in two-dimensional semiconductor diodes. *Nature* **599**, 404–410 (2021).
26. Joe, A. Y. et al. Electrically controlled emission from singlet and triplet exciton species in atomically thin light-emitting diodes. *Phys. Rev. B* **103**, L161411 (2021).
27. Luan, H.-Y. et al. Reconfigurable moiré nanolaser arrays with phase synchronization. *Nature* **624**, 282–288 (2023).
28. Wu, J.-B. et al. Resonant Raman spectroscopy of twisted multilayer graphene. *Nat. Commun.* **5**, 5309 (2014).
29. Xu, C. & Balents, L. Topological superconductivity in twisted multilayer graphene. *Phys. Rev. Lett.* **121**, 087001 (2018).
30. Chen, G. et al. Signatures of tunable superconductivity in a trilayer graphene moiré superlattice. *Nature* **572**, 215–219 (2019).
31. Park, J. M. et al. Tunable strongly coupled superconductivity in magic-angle twisted trilayer graphene. *Nature* **590**, 249–255 (2021).
32. García-Ruiz, A. et al. Electronic Raman scattering in twistrionic few-layer graphene. *Phys. Rev. Lett.* **125**, 197401 (2020).
33. Sarkar, S. et al. Direct bandgap-like strong photoluminescence from twisted multilayer MoS₂ grown on SrTiO₃. *ACS Nano* **14**, 16761–16769 (2020).
34. Leng, Y.-C. et al. Intrinsic effect of interfacial coupling on the high-frequency intralayer modes in twisted multilayer MoTe₂. *Nanoscale* **13**, 9732–9739 (2021).
35. Brzhezinskaya, M. et al. Engineering of numerous Moiré superlattices in twisted multilayer graphene for twistrionics and straintronics applications. *ACS Nano* **15**, 12358–12366 (2021).
36. Lin, X., Zhu, H. & Ni, J. Emergence of intrinsically isolated flat bands and their topology in fully relaxed twisted multilayer graphene. *Phys. Rev. B* **104**, 125421 (2021).
37. Xie, B. et al. Alternating twisted multilayer graphene: generic partition rules, double flat bands, and orbital magnetoelectric effect. *npj Comput. Mater.* **8**, 110 (2022).
38. Nguyen, V. H., Hoang, T. X. & Charlier, J.-C. Electronic properties of twisted multilayer graphene. *J. Phys. Mater.* **5**, 034003 (2022).
39. Park, J. M. et al. Robust superconductivity in magic-angle multilayer graphene family. *Nat. Mater.* **21**, 877–883 (2022).
40. Saumya, K., Naskar, S. & Mukhopadhyay, T. ‘Magic’ of twisted multilayered graphene and 2D nano-heterostructures. *Nano Futures* **7**, 032005 (2023).
41. Agarwal, B. K. *X-Ray Spectroscopy: An Introduction* (Springer, 2013).
42. Zimmermann, P. et al. Modern X-ray spectroscopy: XAS and XES in the laboratory. *Coord. Chem. Rev.* **423**, 213466 (2020).
43. Woolfson, M. M. *An Introduction to X-Ray Crystallography* (Cambridge Univ. Press, 1997).
44. Flack, H. D. & Bernardinelli, G. The use of X-ray crystallography to determine absolute configuration. *Chirality* **20**, 681–690 (2008).
45. Maveyraud, L. & Mourey, L. Protein X-ray crystallography and drug discovery. *Molecules* **25**, 1030 (2020).
46. Withers, P. J. et al. X-ray computed tomography. *Nat. Rev. Methods Prim.* **1**, 18 (2021).
47. Hanke, R., Fuchs, T. & Uhlmann, N. X-ray based methods for non-destructive testing and material characterization. *Nucl. Instrum. Methods Phys. Res. Sect. A* **591**, 14–18 (2008).
48. Yaffe, M. J. & Rowlands, J. A. X-ray detectors for digital radiography. *Phys. Med. Biol.* **42**, 1–39 (1997).
49. Kamino, Y. et al. Development of a four-dimensional image-guided radiotherapy system with a gimbaled X-ray head. *Int. J. Radiat. Oncol. Biol. Phys.* **66**, 271–278 (2006).
50. Li, R. J. et al. Real-time volumetric image reconstruction and 3D tumor localization based on a single x-ray projection image for lung cancer radiotherapy. *Med. Phys.* **37**, 2822–2826 (2010).
51. Uschmann, I. A free-electron laboratory coherent X-ray source. *Nat. Photonics* **14**, 655–656 (2020).
52. Shentcic, M. et al. Tunable free-electron X-ray radiation from van der Waals materials. *Nat. Photonics* **14**, 686–692 (2020).
53. Rodriguez, J. -I. Parametric X-ray methods use 2D heterostructures to generate compact, tunable X-ray sources. *SciLight* **2021**, 281103 (2021).
54. Wong, L. J. & Kammer, I. Prospects in x-ray science emerging from quantum optics and nanomaterials. *Appl. Phys. Lett.* **119**, 130502 (2021).
55. Balanov, A. et al. Temporal and spatial design of x-ray pulses based on free-electron–crystal interaction. *APL Photonics* **6**, 070803 (2021).
56. Huang, S. et al. Enhanced versatility of table-top X-rays from Van der Waals structures. *Adv. Sci.* **9**, 2105401 (2022).
57. Huang, S. et al. Quantum recoil in free-electron interactions with atomic lattices. *Nat. Photonics* **17**, 224–230 (2023).
58. Shi, X. et al. Free-electron interactions with van der Waals heterostructures: a source of focused X-ray radiation. *Light Sci. Appl.* **12**, 148 (2023).

59. Smith, S. J. & Purcell, E. M. Visible light from localized surface charges moving across a grating. *Phys. Rev.* **92**, 1069 (1953).
60. Gover, A., Dvorkis, P. & Elisha, U. Angular radiation pattern of Smith–Purcell radiation. *J. Opt. Soc. Am. B* **1**, 723–728 (1984).
61. Friedman, A. et al. Spontaneous and stimulated emission from quasifree electrons. *Rev. Mod. Phys.* **60**, 471–535 (1988).
62. Adamo, G. et al. Light well: a tunable free-electron light source on a chip. *Phys. Rev. Lett.* **104**, 024801 (2010).
63. Glotin, F. et al. Tunable X-rays generation in a free-electron laser by intracavity Compton backscattering. *Nucl. Instrum. Methods Phys. Res. Sect. A* **393**, 519–524 (1997).
64. Pellegrini, C., Marinelli, A. & Reiche, S. The physics of x-ray free-electron lasers. *Rev. Mod. Phys.* **88**, 015006 (2016).
65. Prat, E. et al. An X-ray free-electron laser with a highly configurable undulator and integrated chicane for tailored pulse properties. *Nat. Commun.* **14**, 5069 (2023).
66. Karagodsky, V., Schieber, D. & Schächter, L. Enhancing X-ray generation by electron-beam–laser interaction in an optical Bragg structure. *Phys. Rev. Lett.* **104**, 024801 (2010).
67. Niknejadi, P. et al. Free-electron laser inverse-Compton interaction x-ray source. *Phys. Rev. Accel. Beams* **22**, 040704 (2019).
68. Popmintchev, T. et al. Phase matching of high harmonic generation in the soft and hard X-ray regions of the spectrum. *Proc. Natl Acad. Sci. USA* **106**, 10516–10521 (2009).
69. Popmintchev, D. et al. Ultraviolet surprise: efficient soft x-ray high-harmonic generation in multiply ionized plasmas. *Science* **350**, 1225–1231 (2015).
70. Rosolen, G. et al. Metasurface-based multi-harmonic free-electron light source. *Light Sci. Appl.* **7**, 64 (2018).
71. Johnson, A. S. et al. Attosecond soft X-ray high harmonic generation. *Philos. Trans. R. Soc. A Math. Phys. Eng. Sci.* **377**, 20170468 (2019).
72. Wong, L. J. et al. Towards graphene plasmon-based free-electron infrared to X-ray sources. *Nat. Photonics* **10**, 46–52 (2015).
73. Rivera, N., Wong, L. J., Joannopoulos, J. D., Soljačić, M. & Kaminer, I. Light emission based on nanophotonic vacuum forces. *Nat. Phys.* **15**, 1284–1289 (2019).
74. Talebi, N. Interaction of electron beams with optical nanostructures and metamaterials: from coherent photon sources towards shaping the wave function. *J. Opt.* **19**, 103001 (2017).
75. Gover, A. & Yariv, A. Free-electron–bound-electron resonant interaction. *Phys. Rev. Lett.* **124**, 064801 (2020).
76. Zhao, Z. X., Sun, X. Q. & Fan, S. H. Quantum entanglement and modulation enhancement of free-electron–bound-electron interaction. *Phys. Rev. Lett.* **126**, 233402 (2021).
77. Kfir, O., Di Giulio, V., de Abajo, F. J. G. & Ropers, C. Optical coherence transfer mediated by free electrons. *Sci. Adv.* **7**, eabf6380 (2021).
78. Lim, J. et al. Quantum interference between fundamentally different processes is enabled by shaped input wavefunctions. *Adv. Sci.* **10**, 2205750 (2023).
79. Dahan, R. et al. Creation of optical cat and GKP states using shaped free electrons. *Phys. Rev. X* **13**, 031001 (2023).
80. Wong, L. J. et al. Control of quantum electrodynamical processes by shaping electron wavepackets. *Nat. Commun.* **12**, 1700 (2021).
81. Wong, L. W. W. et al. Free-electron crystals for enhanced X-ray radiation. *Light Sci. Appl.* **13**, 29 (2024).
82. Wang, Y. H. & Gedik, N. Electron pulse compression with a practical reflectron design for ultrafast electron diffraction. *IEEE J. Sel. Top. Quantum Electron.* **18**, 140–147 (2012).
83. Graves, W. S. et al. Intense superradiant X rays from a compact source using a nanocathode array and emittance exchange. *Phys. Rev. Lett.* **108**, 263904 (2012).
84. Kreier, D., Sabonis, D. & Baum, P. Alignment of magnetic solenoid lenses for minimizing temporal distortions. *J. Opt.* **16**, 075201 (2014).
85. Zhu, J. et al. Formation of compressed flat electron beams with high transverse-emittance ratios. *Phys. Rev. Spec. Top. Accel. Beams* **17**, 084401 (2014).
86. Lim, J., Chong, Y. & Wong, L. J. Terahertz-optical intensity grating for creating high-charge, attosecond electron bunches. *N. J. Phys.* **21**, 033020 (2019).
87. Tang, J. Y. et al. Laguerre-Gaussian mode laser heater for microbunching instability suppression in free-electron lasers. *Phys. Rev. Lett.* **124**, 134801 (2020).
88. Cesar, D. et al. Electron beam shaping via laser heater temporal shaping. *Phys. Rev. Accel. Beams* **24**, 110703 (2021).
89. Chirita Mihaila, M. C. et al. Transverse electron-beam shaping with light. *Phys. Rev. X* **12**, 031043 (2022).
90. Tsesses, S. et al. Tunable photon-induced spatial modulation of free electrons. *Nat. Mater.* **22**, 345–352 (2023).
91. Shiloh, R. et al. Sculpturing the electron wave function using nanoscale phase masks. *Ultramicroscopy* **144**, 26–31 (2014).
92. Grünewald, L. et al. Fabrication of phase masks from amorphous carbon thin films for electron-beam shaping. *Beilstein J. Nanotechnol.* **10**, 1290–1302 (2019).
93. Shiloh, R. et al. Nanostructuring of electron beams. *Phys. Scr.* **94**, 034004 (2019).
94. Verbeeck, J. et al. Demonstration of a 2×2 programmable phase plate for electrons. *Ultramicroscopy* **190**, 58–65 (2018).
95. Yu, C.-P., Vega Ibañez, F., Béché, A. & Verbeeck, J. Quantum wavefront shaping with a 48-element programmable phase plate for electrons. *SciPost Phys.* **15**, 223 (2023).
96. Salvat, F. et al. Analytical Dirac–Hartree–Fock–Slater screening function for atoms ($Z = 1–92$). *Phys. Rev. A* **36**, 467 (1987).
97. Salvat, F. Elastic scattering of fast electrons and positrons by atoms. *Phys. Rev. A* **43**, 578 (1991).
98. Peskin, M. E. *An Introduction to Quantum Field Theory* (CRC Press, 1995).

Acknowledgements

This project is supported by the Ministry of Education, Singapore (Project ID MOE-T2EP50222-0012).

Author contributions

All authors made critical contributions to the manuscript.

Competing interests

The authors declare no competing interests.

Additional information

Supplementary information The online version contains supplementary material available at <https://doi.org/10.1038/s44310-024-00043-4>.

Correspondence and requests for materials should be addressed to Liang Jie Wong.

Reprints and permissions information is available at <http://www.nature.com/reprints>

Publisher's note Springer Nature remains neutral with regard to jurisdictional claims in published maps and institutional affiliations.

Open Access This article is licensed under a Creative Commons Attribution-NonCommercial-NoDerivatives 4.0 International License, which permits any non-commercial use, sharing, distribution and reproduction in any medium or format, as long as you give appropriate credit to the original author(s) and the source, provide a link to the Creative Commons licence, and indicate if you modified the licensed material. You do not have permission under this licence to share adapted material derived from this article or parts of it. The images or other third party material in this article are included in the article's Creative Commons licence, unless indicated otherwise in a credit line to the material. If material is not included in the article's Creative Commons licence and your intended use is not permitted by statutory regulation or exceeds the permitted use, you will need to obtain permission directly from the copyright holder. To view a copy of this licence, visit <http://creativecommons.org/licenses/by-nc-nd/4.0/>.

© The Author(s) 2024